

SWASH HYDRODYNAMIC MODELLING USING CROCO: VALIDATION ON NHA TRANG EXPERIMENT

Rachid Benshila¹, Luis Pedro Almeida², Francis, Auclair³, Rafael Almar⁴, Cyril Nguyen⁵ and Patrick Marchesiello⁴

Abstract

The swash zone is one of the most dynamic regions in the nearshore. During storms the beach response (erosion and recovery) is strongly controlled by the swash zone and for this reason it is crucial to acquire field data to and develop new modeling solutions to improve the forecast of the processes in this zone. New remote sensing techniques, such as 2D Lidar, that can measure swash hydro- and morphodynamics provide extremely valuable observations to develop and validate numerical models. In the present work a novel dataset of swash hydrodynamic observations (performed by a 2D Lidar) are used to test the performance of a new non-hydrostatic tri-dimensional numerical model (CROCO) to predict wave transformation and swash motions on a sandy beach with a low tide terrace (Nha Trang, Vietnam). A high resolution grid was setup, covering the entire swash zone and the inner surf zone. Comparisons between CROCO and 2D Lidar indicate that despite some differences between individual waves characteristics (length of swash excursions and durations) in the overall the model show skills to predict extreme run-up statistics with very high level of accuracy.

Key words: Nearshore modelling, Swash zone dynamics, Wave resolving, Foreshore.

1. Dataset

A field experiment was undertaken between 26 November and 04 December 2015 at Nha Trang beach, a sandy beach located on a semi-closed bay on the South East of Vietnam (Figure 1). This medium-to-coarse sandy beach ($D_{50}=0.3$ mm) has a fairly steep beach face slope (~ 0.1) and a narrow (~ 40 m) alongshore uniform and flat (~ 0.01) low tide terrace (LTT). A 2D Lidar (SICK LMS500) deployed on top of a metallic tower (Figure 1) to measure high frequency (4 Hz), and high resolution (average distance between points is about 10 cm) swash zone hydrodynamics (swash position and depth) and morphological evolution along a cross-shore section of the beach.

¹CNRS/LEGOS, Toulouse, France. rachid.benshila@legos.obs-mip.fr

²CNES/LEGOS, Toulouse, France. pedro.almeida@legos.obs-mip.fr

³UPS/LA, Toulouse, France. francis.auclair@aero.obs-mip.fr

⁴IRD/LEGOS, Toulouse, France. rafael.almar@legos.obs-mip.fr and patrick.marchesiello@legos.obs-mip.fr

⁵CNRS/LA, Toulouse, France. cyril.nguyen@aero.obs-mip.fr

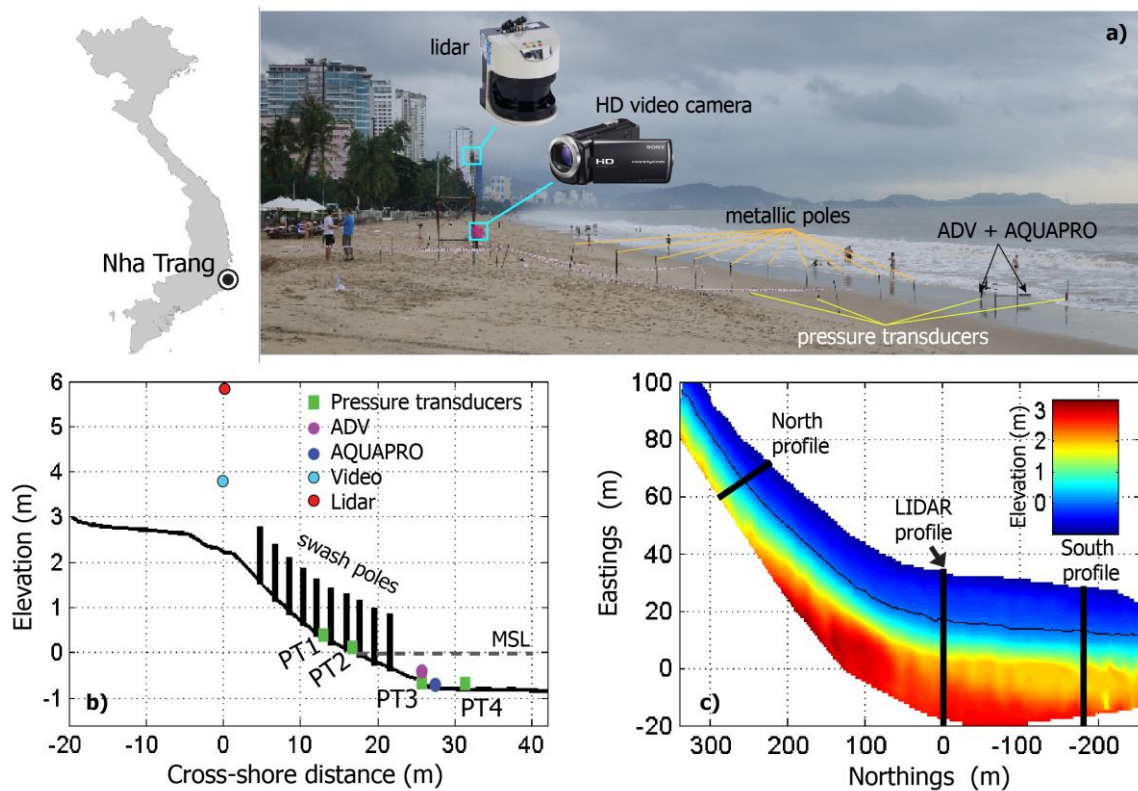


Figure 1. Location and data acquisition system

2. Circulation model framework

3.1. Description

CROCO is the last evolution of ROMS-AGRIF model (PENVEN *et al.*, 2006), part of the ROMS model. It has the particularity of having nesting capabilities and a non-hydrostatic option (not used here). Initially developed for basin scale modeling (O10 km), its use has recently been extended and assessed to nearshore processes resolutions (O10 m, Marchesiello *et al.*, 2015) with phase averaged wave forcing. We propose here to go one range further in resolving decimeter scales processes and solving explicit waves.

CROCO is a three-dimensional, free surface, terrain-following numerical circulation model that solves finite-difference approximations of the Reynolds averaged Navier–Stokes (RANS) equations using originally the hydrostatic and Boussinesq assumptions (Chassignet *et al.*, 2000; Haidvogel *et al.*, 2000) with a split-explicit time stepping algorithm (Shchepetkin and McWilliams, 2005; Haidvogel *et al.*, 2008). It uses a horizontal curvilinear Arakawa C grid and vertical stretched terrain-following coordinates. CROCO has a flexible structure that allows choices for many of the model components, including options for advection schemes (second order, third order, fourth order, and positive definite), turbulence submodels, and boundary conditions. It includes bottom and surface boundary layer submodels, air-sea fluxes, surface drifters, a nutrient-phytoplankton-zooplankton model. Momentum, scalar advection, and diffusive processes are represented using transport equations. The density field is determined from an equation of state that accounts for temperature, salinity, and suspended-sediment concentrations. In this paper, the term constant refers to values that are time-invariant, and the term uniform refers to values that do not vary in space. Recently original non-hydrostatic capabilities have been developed (Auclair, 2010): instead of solving the classical Poisson problem with pressure correction, the Boussinesq assumption is relaxed. This allows the embedding of the non-hydrostatic mode inside the external mode, using a time stepping technic.

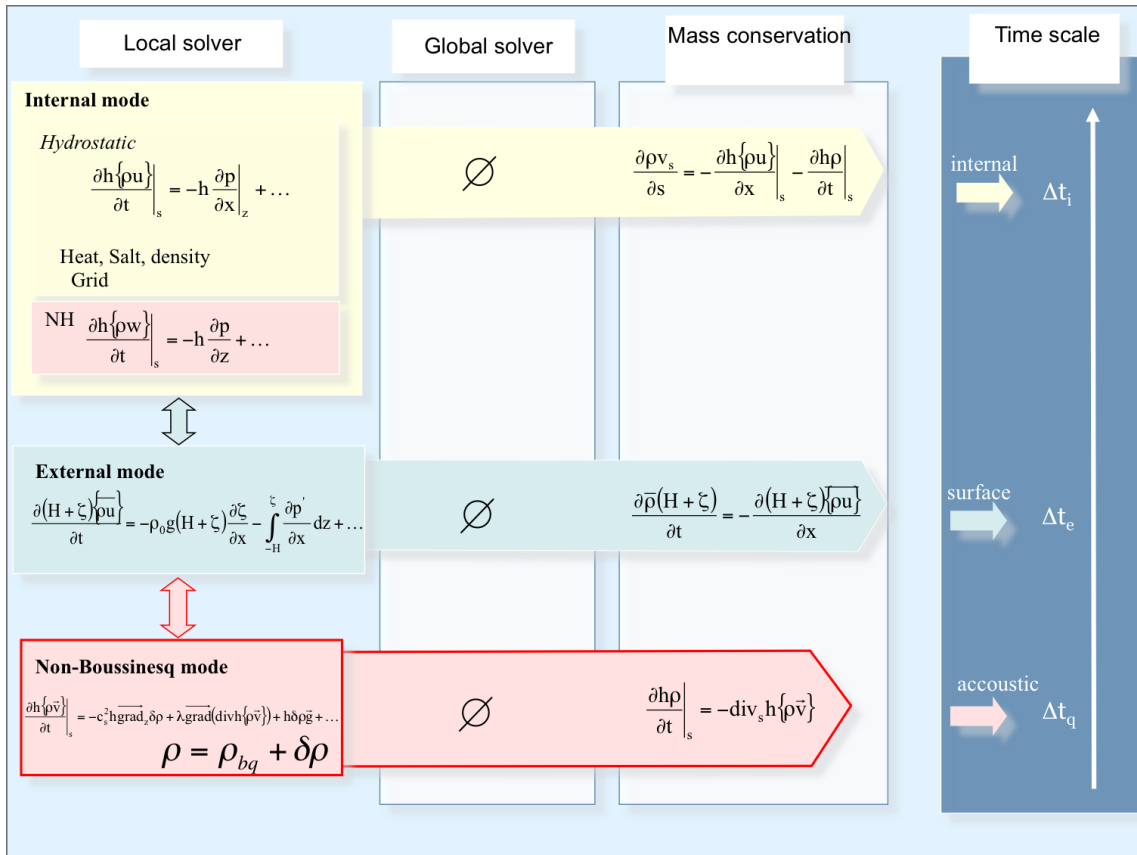


Figure 2. Algorithm of the non-Boussinesq solver with the embedded resolution of the three different modes

The governing equations (1)–(4) are presented in flux form, in Cartesian horizontal coordinates and sigma vertical coordinates. For curvilinear grids, additional metric terms appear (Haidvogel et al., 2000) that are not shown here. In the particular case of a x-z section for a fluid with uniform density, the classical primitives equations become for the momentum (here for the hydrostatic case):

$$\frac{\partial(H_z u)}{\partial t} + \frac{\partial(u H_z u)}{\partial x} + \frac{\partial(\Omega H_z u)}{\partial s} = -\frac{H_z}{\rho_0} \frac{\partial p}{\partial x} - H_z g \frac{\partial \eta}{\partial x} - \frac{\partial}{\partial s} \left[\frac{(K_M + \nu)}{H_z} \frac{\partial u}{\partial s} \right] + \mathcal{F}_u + \mathcal{D}_u \quad (1)$$

$$0 = -\frac{1}{\rho_0} \frac{\partial p}{\partial s} - \frac{g}{\rho_0} H_z \rho \quad (2)$$

for the mass conservation:

$$\frac{\partial \eta}{\partial t} + \frac{\partial(H_z u)}{\partial x} + \frac{\partial(H_z \Omega)}{\partial s} = 0 \quad (3)$$

and for the tracer transport (if any, otherwise density):

$$\frac{\partial(H_z C)}{\partial t} + \frac{\partial(u H_z C)}{\partial x} + \frac{\partial(\Omega H_z C)}{\partial s} = -\frac{\partial}{\partial s} \left[\frac{K_{\theta+\nu\theta}}{H_z} \frac{\partial u v}{\partial s} \right] + C_{source} \quad (4)$$

with u, Ω the velocity components in the (x, s) referential, H_z the level thickness, p the pressure, ρ the density anomaly, ρ_0 the reference density, g the gravity, η the free surface elevation, ν the molecular viscosity, K_M the vertical eddy viscosity, \mathcal{F}_u and \mathcal{D}_u the forcing terms and the horizontal. In the non-hydrostatic case, the vertical momentum equation becomes a combination of (1) and (2), substituting w to u .

3.2. Specific model settings

For model calibration at Nha Trang we set up first one configuration corresponding to the observations presented in Figure 1, covering an extent of 30 m, at 0.1 m resolution. The model is only forced at its offshore boundary by water elevation time series at 4Hz frequency. The model configuration used in this simulations were standard for regional configurations, see Table 1 for a description.

With this setting the 3D equations 1, 2 and 3, are solved without forcing terms ($\mathcal{F}_u = 0$). The vertical dissipation (K_M) is set constant and the explicit horizontal eddy viscosity (\mathcal{D}_u) is given by the flow- and resolution-dependent Smagorinski (Smagorinski, 1963):

$$\nu = (C_s \Delta x)^2 |S| \quad (5)$$

where S is the strain rate, Δx the model resolution and C_s the Smagorinsky constant. Such formulation allows to turn on the dissipation only when the shear becomes critical.

An additional viscosity term ν_b is added to take into account the wave breaking, following the work done with Boussinesq models (Kennedy et al, 2000), such as:

$$\nu_b = B \delta_b (h + \eta) \quad (6)$$

where δ_b is a mixing length coefficient, h and η the reference water level and the elevation, and B a coefficient varying smoothly from 0 to 1, depending on the slope.

For the bottom friction we use a logarithmic formulation, assuming that the flow in the bottom boundary layer has the classic vertical profile defined by a shear velocity u_* and bottom roughness length z_0 as:

$$|u| = \frac{u_*}{\mathcal{K}} \ln\left(\frac{z}{z_0}\right) \quad (7)$$

with $|u|$ the module of the speed, u_* is the friction velocity, z is the elevation above the bottom, \mathcal{K} is von Karman's constant and z_0 a constant bottom roughness length. The advantage of this approach is that the velocity and the vertical elevation of that velocity are used in the equation. Because the vertical elevation of the velocity in the bottom computational cell will vary spatially and temporally, the inclusion of the elevation provides a more consistent formulation.

Model Parameters	Exp1	Exp2
Domain length	30 m	1200 m
Spatial resolution	0.1 m	0.5 m
Number of vertical levels	5	10
Time step	0.01 s	0.05 s
Vertical viscosity	0.001 m ² s ⁻¹	0.001 m ² s ⁻¹
Smagorinsky constant	0.01	0.01
Bottom roughness	0.01 m	0.001 m
Duration	10 mn	720 mn

Table 1. Model setting and parameters

4. Results

4.1. Lidar measurements

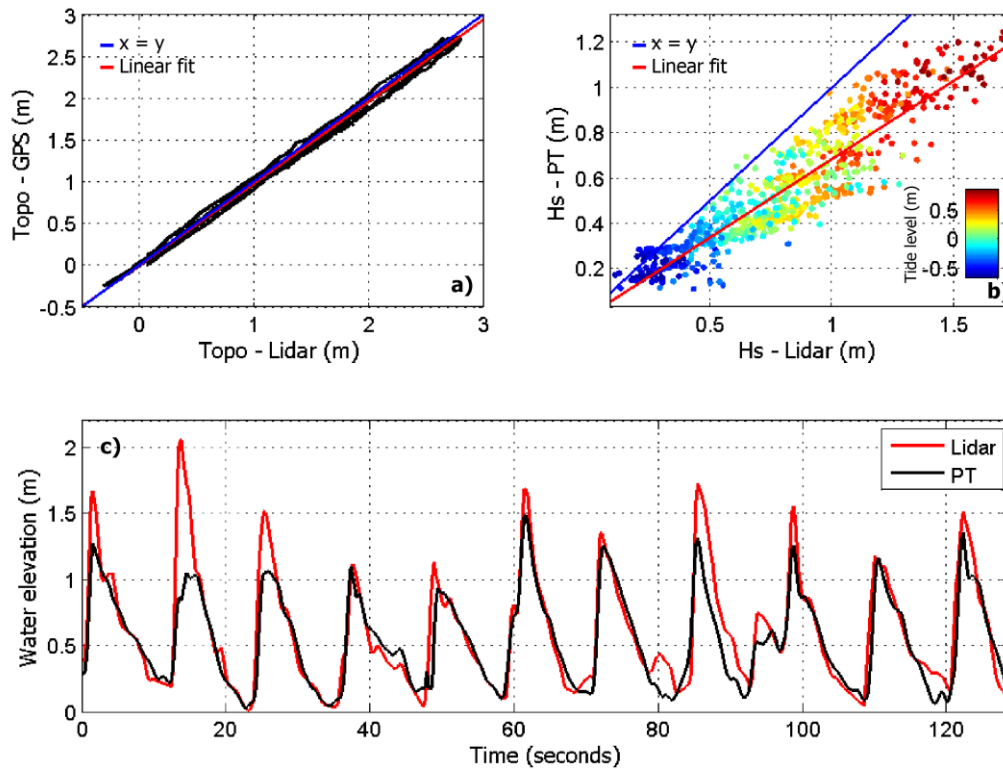


Figure 3. Comparison between significant wave height (Hs) measured by pressure transducer (PT) and Lidar (top left figure); and scatter plot of the comparison between the topographic measurements performed by the RTK-GPS and Lidar (top right figure). Time series of water elevation from Lidar and at PTs

Lidar observations (water levels and topography) were compared with *in situ* measurements obtained by traditional techniques (pressure transducer for water levels and Real Time Kinematic GPS), in order to evaluate the accuracy of this novel remote sensing method. Results are presented in Figure 3 and show that wave observations performed by the Lidar have a very good correlation with correlation coefficient (r^2) of 0.84 and root mean squared error (*rmse*) of about 0.1 m. The results also show that Lidar observation tend to over estimate the observations performed by the PT, which is potentially due to the typical underestimation that PT have under very shallow water where a large amount of air mixed in the water perturbs pressure measurements. The comparisons made with the topographic observations (Figure 3) are significantly better, with a r^2 of 0.99 and *rmse* of 0.05 m, which is an error in the order of the magnitude of the GPS accuracy (± 5 cm).

4.2. Model tests cases

To assess the model results, we proceed in two steps with an incremental approach in term of complexity. We first choose to test the model ability to reproduce the evolution of the water line in a very controlled experiment (hereafter calibration phase), then to investigate the results of the model when modeling a full tide period (hereafter model evaluation). Settings of the two experiments are summarized in table 1.

4.2.1. Case 1: model calibration

Model results are compared with field observations (Lidar) for the first test case (Figure 4). The simulated area is the upper beach part as shown on figure 1, with a length of 30 meters, where we consider that most of the waves have already broken. The aim of this test is to assess the ability of the model to deal with wet and drying areas, wave propagation and reflection. The wave breaking parameterization described equation (6) is activated but not really tested here, as well as waves transformations, so the simulation is performed in hydrostatic mode only. This configuration is used to test and calibrate model parameters such as bottom friction of viscosity (tests not shown here) to be used for test case 2, final settings are shown table 1.

The model has been run with a threshold of 1cm centimeter under which a cell is considered as dry (where the outgoing mass flux is set temporarily to zero). It is forced by Lidar data at its offshore boundary. The model shows good agreement with the observation. Regarding the raw time series, the model tends to miss several high frequency swash excursions, with predicted excursions showing smaller amplitude of variation compared with observations (Figure 4). Swash excursion has an apparent larger duration in the model, which can be explained by an underestimation of the backwash velocity.

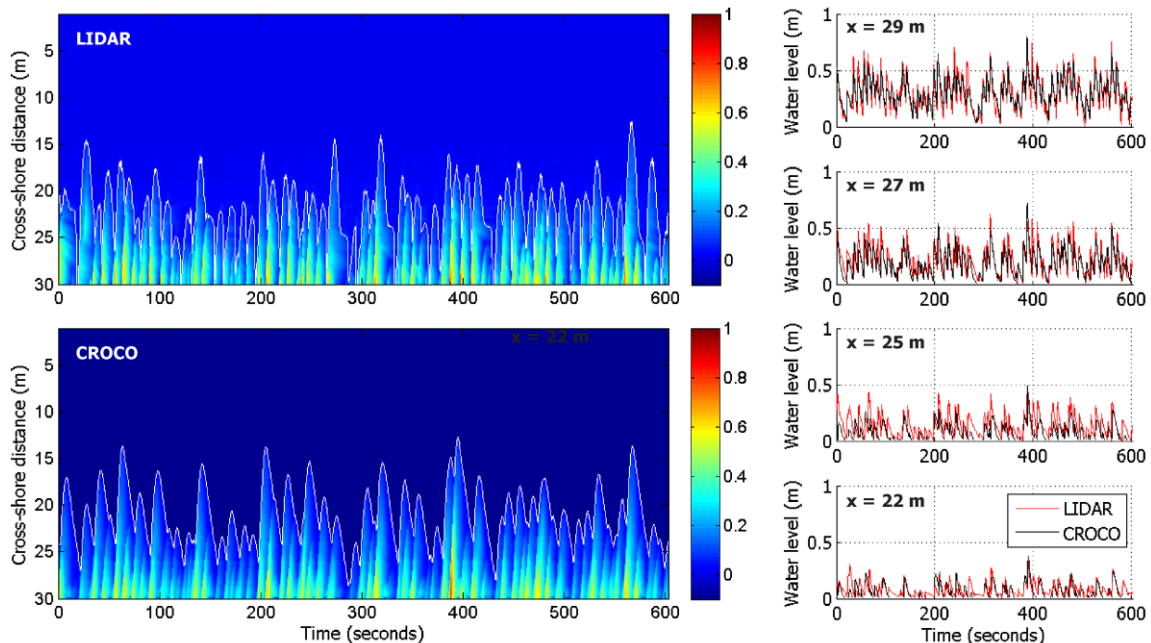


Figure 4. Model results for Case 1: comparison of Lidar observations and model results. Evolution of the water line on a sample period of 10mn (left panel) and time series of water level at different locations (right panel)

If we consider the Lidar data evaluation (Figure 3.) and the left panel (Figure 4.), we note that the model mostly under-evaluate the water level in shallow areas (x=22m) where we note an over estimation of the Lidar compared to the PTs.

4.2.2. Case 2: model evaluation

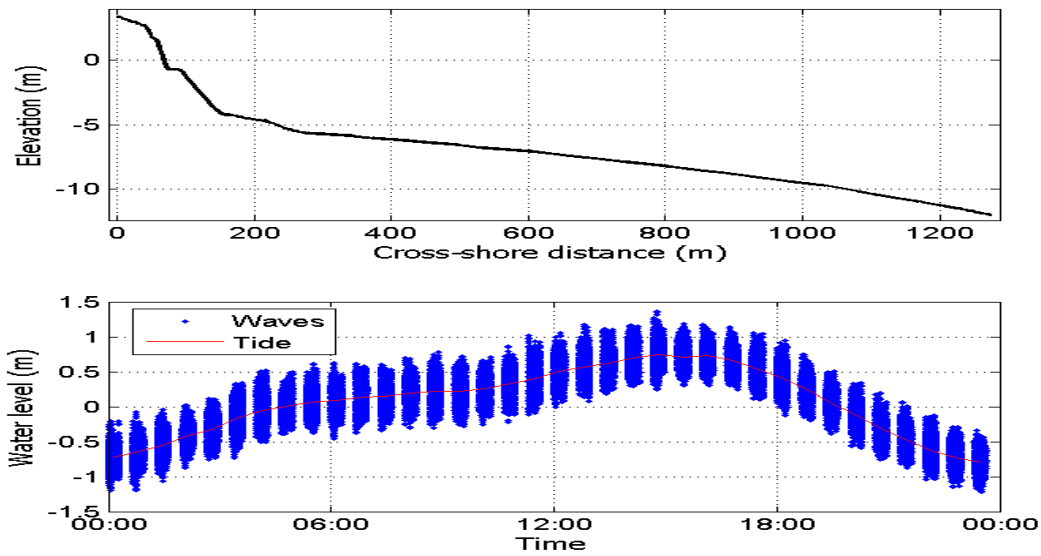


Figure 5. Spatial domain and water level for case test 2

The model evaluation corresponds to a simulation performed on a large domain (1200m) forced at the offshore boundary by ADCP data at 2 Hz. It is run in non-hydrostatic mode to capture properly wave transformation and breaking point. The duration corresponds to a full tidal period to assess the model behavior under different hydrodynamic regimes. Experiment characteristics are summarized Table 1. and Figure 5.

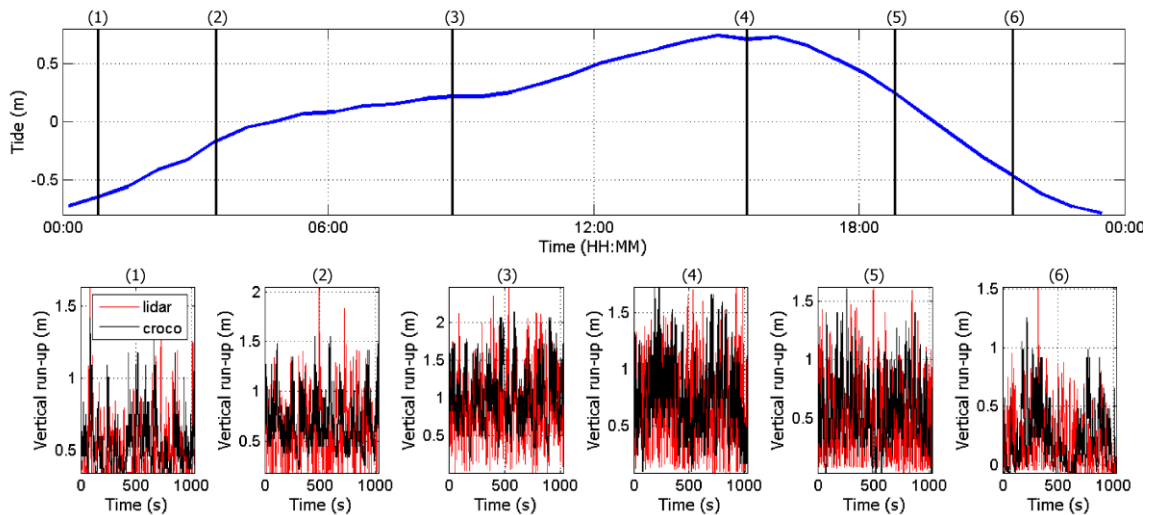


Figure 6. Model-Data comparison at different time

Figure 6. presents model Lidar run-up comparison at different time with different tidal level and under different wave conditions. As shown previously, the model tends to underestimate the water level for extreme events. This is confirmed by figure 7. with the comparison of the significant vertical run-up between the model and the Lidar. As previously we can argue that the Lidar tends to overestimate the water level in very shallow areas since Figure 7. is very similar to Figure 3. Thus it may also indicate the model failing to represent properly the bottom friction in those particular areas.

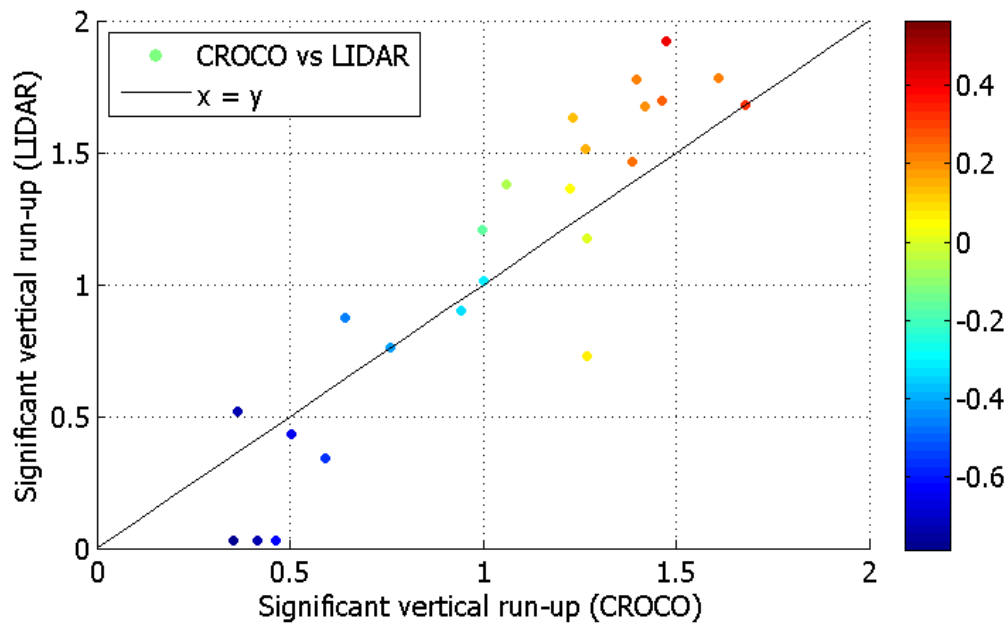


Figure 7. Scatter plot of the significant run-up (Model and Data)

Finally, to go one step further, we proceed to a spectral analysis of the vertical run-up values (Figure 8.) for six 10 mn sequences during the tidal cycle. The model is perfectly able to capture two different behaviors. At low tide (time 1 and 6), the spectrum is characterized by two peaks of frequency, at 0.1 Hz and around 0.01 Hz. At high tide (time 4), only the high frequency remains. The model reproduces also the transition phase with the disappearance of the low frequency peak.

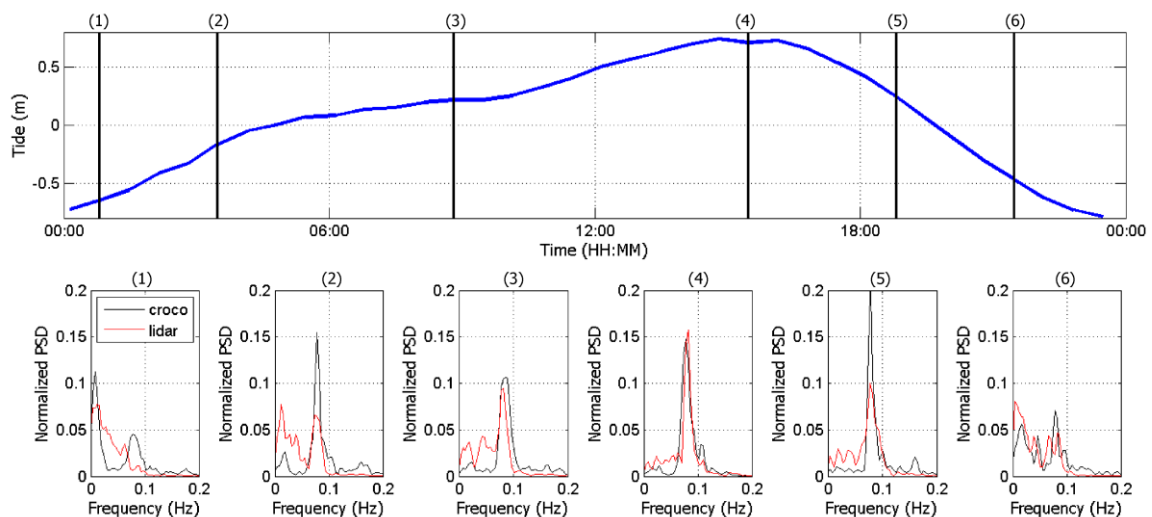


Figure 8. Frequency analysis of the run-up

5. Conclusions and future works

The ability of a tri-dimensional model (CROCO) originally suitable for regional circulation studies to reproduce swash zone motions (swash excursions and depth) was tested against novel measurements performed with a 2D Lidar. In the overall the model is efficient in reproducing swash motions during mild and energetic wave conditions on a sandy beach with a fairly steep beach slope. While wave-by-wave comparisons ind

icate that the model underestimates backwash velocities and misses some higher frequency swash excursions, the run-up statistics show that the model is capable of predicting mean and extreme run-up elevations with a very high level of accuracy. Further work will include sensibility tests with different set of bathymetry to investigate the apparition of low frequency for extreme run-up at low tide.

Acknowledgements

This research has received support from grants by ANR (COASTWAR ANR-14-ASTR-0019) and LEFE/INSU (COMODO-WAVES). It was also granted access to the HPC resources of GENCI-IDRIS under allocation 2017–017298

References

- Auclair F., Estournel C., Floor J. W., Herrmann M., Nguyen C., Marsaleix P., 2011. *A non-hydrostatic algorithm for free-surface ocean modelling*, *Ocean Modelling*, 36, 49-70 <http://dx.doi.org/10.1016/j.ocemod.2010.09.006>
- Chassignet E.P., Arango H.G., Dietrich D., Ezer T., Ghil M., Haidvogel D.B., Ma C.-C., Mehra A., Paiva A.M., Sirkes Z., 2000. DAMEE-NAB: the base experiments. *Dynamics of Atmospheres and Oceans*, Vol. 32, pp 155–183. [http://dx.doi.org/10.1016/S0377-0265\(00\)00046-4](http://dx.doi.org/10.1016/S0377-0265(00)00046-4)
- Haidvogel D.B., Arango H.G., Hedstrom K., Beckmann A., Malanotte-Rizzoli P., Shchepetkin A.F., 2000. Model evaluation experiments in the North Atlantic Basin: Simulations in nonlinear terrain-following coordinates. *Dynamics of Atmospheres and Oceans*, Vol. 32, pp 239–281. [http://dx.doi.org/10.1016/S0377-0265\(00\)00049-X](http://dx.doi.org/10.1016/S0377-0265(00)00049-X)
- Haidvogel D.B., Arango H.G., Budgell W.P., Cornuelle B.D., Curchitser E., Di Lorenzo E., Fennel K., Geyer W.R., Hermann A.J., Lanerolle L., Levin J., McWilliams J.C., Miller A.J., Moore A.M., Powell T.M., Shchepetkin A.F., Sherwood C.R., Signell R.P., Warner J.C., Wilkin J., 2008. Ocean forecasting in terrain-following coordinates: Formulation and skill assessment of the Regional Ocean Modeling System. *Journal of Computational Physics*, Vol. 227(7), pp 3595-3624. <http://dx.doi.org/10.1016/j.jcp.2007.06.016>
- Kennedy A.B., Chen Q., Kirby J.T., Dalrymple R.A., 2000. Boussinesq modeling of wave transformation, breaking, and runup. I: 1D. *Journal of waterway, port, coastal, and ocean engineering*, Vol. 126(1), pp 39-47. [http://dx.doi.org/10.1061/\(ASCE\)0733-950X\(2000\)126:1\(39\)](http://dx.doi.org/10.1061/(ASCE)0733-950X(2000)126:1(39))
- Marchesiello P., Benshila R., Almar R., Uchiyama Y., McWilliams J.C., Shchepetkin A., 2015. On tridimensionnal rip current modeling. *Ocean Modelling*, Vol. 96, pp 36-48. <http://dx.doi.org/10.1016/j.ocemod.2015.07.003>
- Penven P., Debreu L., Marchesiello P., McWilliams J.C., 2006. Evaluation and application of the ROMS 1-way embedding procedure to the central California upwelling system. *Ocean Modelling*, Vol. 12, pp 157-187. <http://dx.doi.org/10.1016/j.ocemod.2005.05.002>
- Shchepetkin A.F., McWilliams J.C., 2005. The regional ocean modeling system (ROMS): a split-explicit, free-surface, topography-following-coordinates ocean model. *Ocean Modelling*, Vol. 9, pp 347–404. <http://dx.doi.org/10.1016/j.ocemod.2004.08.002>
- Smagorinsky J., 1963. General circulation experiments with the primitive equations. *Monthly Weather Review*, Vol. 91(3), pp 99–164. [http://dx.doi.org/10.1175/1520-0493\(1963\)091<0099:GCEWTP>2.3.CO;2](http://dx.doi.org/10.1175/1520-0493(1963)091<0099:GCEWTP>2.3.CO;2)
- Warner J.C., Sherwood C.R., Signell R.P., Harris C.K., Arango H.G., 2008. Development of a three-dimensional, regional, coupled wave, current, and sediment-transport model. *Computers & Geosciences*, Vol. 34, pp 1284–1306. <http://dx.doi.org/10.1016/j.cageo.2008.02.012>